

Controlled-Phase Gate Using Dynamically Coupled Cavities and Optical Nonlinearities

Mikkel Heuck^{1,2,*}, Kurt Jacobs^{3,4,5} and Dirk R. Englund²

¹*DTU Fotonik, Technical University of Denmark, Building 343, 2800 Kongens Lyngby, Denmark*

²*Department of Electrical Engineering and Computer Science, Massachusetts Institute of Technology, 77 Massachusetts Avenue, Cambridge, Massachusetts 02139, USA*

³*U.S. Army Research Laboratory, Computational and Information Sciences Directorate, Adelphi, Maryland 20783, USA*

⁴*Department of Physics, University of Massachusetts at Boston, Boston, Massachusetts 02125, USA*

⁵*Hearne Institute for Theoretical Physics, Louisiana State University, Baton Rouge, Louisiana 70803, USA*



(Received 30 September 2019; accepted 13 March 2020; published 20 April 2020)

We show that relatively simple integrated photonic circuits have the potential to realize a high fidelity deterministic controlled-phase gate between photonic qubits using bulk optical nonlinearities. The gate is enabled by converting travelling continuous-mode photons into stationary cavity modes using strong classical control fields that dynamically change the effective cavity-waveguide coupling rate. This architecture succeeds because it reduces the wave packet distortions that otherwise accompany the action of optical nonlinearities [J. Shapiro, *Phys. Rev. A* **73**, 062305 (2006); J. Gea-Banacloche, *Phys. Rev. A* **81**, 043823 (2010)]. We show that high-fidelity gates can be achieved with self-phase modulation in $\chi^{(3)}$ materials as well as second-harmonic generation in $\chi^{(2)}$ materials. The gate fidelity asymptotically approaches unity with increasing storage time for an incident photon wave packet with fixed duration. We also show that dynamically coupled cavities enable a trade-off between errors due to loss and wave packet distortion. Our proposed architecture represents a new approach to practical implementation of quantum gates that is room-temperature compatible and only relies on components that have been individually demonstrated.

DOI: [10.1103/PhysRevLett.124.160501](https://doi.org/10.1103/PhysRevLett.124.160501)

The quest for deterministic photon-photon logic gates has generally been hindered by the absence of sufficiently strong nonlinearities at optical frequencies. One possible solution is to use detection as an effective nonlinearity [1], but two-qubit gates realized this way are probabilistic and require large resource overheads [2]. Even with large Kerr nonlinearities, Shapiro showed in 2006 that two-photon gates between traveling wave packets cannot achieve high fidelity [3]; this fundamental limit was further elucidated in Refs. [4–7], shedding doubt on the possibility of quantum computing with bulk nonlinearities. Recent theoretical proposals have reopened the discussion by showing that arbitrarily high fidelity is possible in certain limits, but their implementations require cryogenically cooled identical quantum emitters [8,9], atomic ensembles [10], or nonlocal nonlinearities [11,12].

Here, we introduce a new approach that achieves near-unity gate fidelity in a compact and room-temperature compatible architecture, which only relies on the bulk nonlinearities of optical cavities realized in common materials for photonic integrated circuits. The scheme relies on two-photon interactions when the photons are dynamically stored in a nanophotonic cavity. Figure 1 illustrates the concept for $\chi^{(2)}$ and $\chi^{(3)}$ nonlinearities in photonic crystal (PHC) cavities. Photons with carrier frequency ω_a (purple) travel in a waveguide and couple

to cavity mode a (also at ω_a as shown in the bottom panel of Fig. 1) with a static rate, γ . In the $\chi^{(2)}$ example, mode b (red) is decoupled from the waveguide and couples to mode a through a three wave mixing interaction controlled by a strong classical field occupying a mode at ω_p (green), such that $\omega_p + \omega_b = \omega_a$. Adjusting the amplitude and phase of the control field results in a time-dependent effective coupling between mode b and the waveguide that enables complete absorption and emission of specifically shaped wave packets. If two photons are absorbed into mode b , the quantum state undergoes Rabi oscillations between two photons in mode b and one photon in mode c at $2\omega_b$ (blue). Adjusting the storage time to equal one full Rabi oscillation introduces a π phase compared to storing a single photon in mode b , which accomplishes the conditional phase operation. For a $\chi^{(3)}$ nonlinearity, modes a and b are coupled through four wave mixing using two classical control fields at ω_1 and ω_2 such that $\omega_2 - \omega_1 = \omega_a - \omega_b$. The conditional phase shift arises from self-phase modulation of two photons in mode b , which is absent for a single-photon input. Dynamically coupled cavities are also useful for manipulating wave packets of individual photons as illustrated by a recent proposal for separating temporal modes of propagating photons [13].

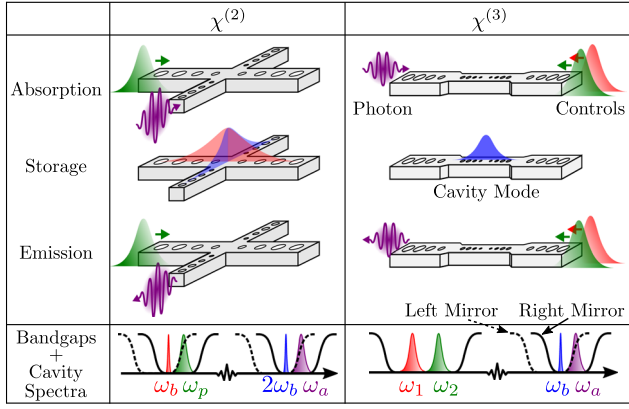


FIG. 1. Absorption, storage, and emission process with schematic illustrations of cavity implementations in $\chi^{(2)}$ (left) and $\chi^{(3)}$ (right) materials. Two sets of photonic crystal mirrors oriented perpendicularly ($\chi^{(2)}$) or inline ($\chi^{(3)}$) have band gaps in different frequency ranges as illustrated by the black lines in the bottom panel. One-sided cavities required for complete absorption are achieved by a slight frequency offset between the band gaps of the right (solid black) and left (dashed black) mirror. The decoupled mode (blue) is within the band gap of both mirrors while the coupled mode (purple) lies at the band edge of the left mirror. Only the decoupled cavity modes must have small volumes for efficient photon-photon interaction. The control modes are confined by weak mirrors (ω_1 and ω_2) located at the exterior of the small cavity modes.

While stored in decoupled cavity modes, photons are single mode in the limit of zero intrinsic cavity loss. The fidelity limitations pointed out in Ref. [3] therefore do not apply to their interaction during this time. However, the control field that optimally absorbs and emits wave packets depends on the photon number when nonlinear interactions are present during the absorption and emission process. Since the same control field must be applied to any input state, it unavoidably introduces a finite amount of error consistent with Refs. [3–7]. Crucially, our numerical analysis reveals that this error scales favorably with the ratio between the storage time, T , and the duration of the input wave packet.

Our CPHASE gate works with either a dual- or single-rail encoding. For the former, two waveguides that carry the logical 1 for each qubit are in the joint state $|11\rangle$ if and only if both qubits are logical 1. Applying a 50/50 directional coupler to these waveguides transforms this joint state to $(|02\rangle + |20\rangle)/\sqrt{2}$. Each waveguide feeds an identical copy of either version of our one-sided cavity structure illustrated in Fig. 1. Thus two photons are loaded into one of the two cavities if and only if both input qubits are logical 1. The two waveguides that code for logical 0 are also each terminated by a copy of our one-sided cavity to ensure a consistent phase shift among the other logical states. For an illustration of this waveguide configuration, see, e.g., Ref. [14]. In this circuit, the phase difference between

one- and two-photon wave packets incident on the cavities ensures the logical gate operation. We denote the action of the gate using bars (e.g., $|01\rangle \rightarrow |\bar{0}\bar{1}\rangle$). Single-photon input states like $|1\rangle = \int dt \xi_{\text{in}}(t) \hat{w}^\dagger(t) |\emptyset\rangle$ are fully characterized by their wave packets, $\xi_{\text{in}}(t)$, where normalization requires $\int |\xi_{\text{in}}(t)|^2 dt = 1$ and $\hat{w}(t)$ is the continuous-time annihilation operator of the waveguide. Output wave packets are defined through $|\bar{1}\rangle = \int dt \xi_{\text{out}}(t) \hat{w}^\dagger(t) |\emptyset\rangle$ or $|\bar{1}\bar{1}\rangle = \int \int dt_m dt_n \xi_{\text{out}}(t_m, t_n) \hat{w}^\dagger(t_m) \hat{w}^\dagger(t_n) |\emptyset\rangle$ corresponding to the input $|11\rangle$. With identical cavities at the end of all four waveguides, states $|00\rangle$, $|01\rangle$, and $|0\bar{1}\rangle$ acquire the same phase. The controlled-phase operation therefore corresponds to the phase requirement, $\arg(\langle 0|\bar{0}\rangle) = \arg(\langle 1|\bar{1}\rangle) = \arg(\langle 11|\bar{1}\bar{1}\rangle) + \pi/2$, and we define the one- and two-photon state fidelities as

$$F_1 = |\langle 1|\bar{1}\rangle|^2 = \left| \int \xi_{\text{out}}(t)^* \xi_{\text{in}}(t-T) dt \right|^2 \quad (1a)$$

$$F_{11} = \left| \int \int \xi_{\text{out}}(t_m, t_n)^* \xi_{\text{in}}(t_n-T) \xi_{\text{in}}(t_m-T) dt_n dt_m \right|^2. \quad (1b)$$

We include a loss rate, γ_L , for all cavity modes. The output is therefore in a mixed state but we only calculate the dynamics of the zero-loss subspace so that the output states above are not normalized, and the fidelities in Eq. (1) become lower bounds on the fidelities [15].

To calculate the output wave packets, we use a Schrödinger-picture version of the established time-bin formalism [16–18], which allows us to derive explicit equations of motion for the cavity states and input-output relations in terms of the cavity Fock basis. In the time-bin formulation the waveguide field is divided into N time bins of duration Δt , and the cavity interacts with the time bins one after the other. We refer to Ref. [15] for detailed derivations of all the equations of motion and input-output relations used here.

In time bin n , the classical control field that couples modes a and b is $\Lambda_n^{(k)}$, where (k) refers to a $\chi^{(k)}$ material. In Ref. [15] we derived explicit solutions for $\Lambda_n^{(k)}$ that enable complete absorption of a single photon with an arbitrary wave packet or emission of an arbitrary output. The solutions differ due to cross-phase-modulation imparted on cavity modes a and b by the control fields only in $\chi^{(3)}$ materials. Figure 2(a) shows an example of the absorption process with ξ_{in} being a Gaussian centered at T_{in} with temporal full-width-at-half-maximum τ_G and spectral width Ω_G . The occupation probability of mode b is $P_{01}^{(k)}$, where k again refers to the order of the nonlinearity. $\Lambda^{(3)}$ has a time-dependent phase to compensate for the cross-phase-modulation it induces on modes a and b . This broadens and shifts its Fourier spectrum as seen in Fig. 2(b). The absence

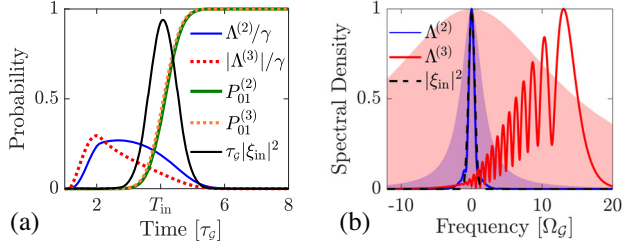


FIG. 2. (a) Absorption of a Gaussian wave packet including the solution of $\Lambda^{(k)}$ for both $\chi^{(2)}$ and $\chi^{(3)}$ materials. (b) Fourier transformations of $\Lambda^{(k)}(t)$ from (a). The shaded areas plot Lorentzian resonances of mode a with linewidths $\gamma/\Omega_G = 6$ for a $\chi^{(2)}$ material (blue) and $\gamma/\Omega_G = 30$ for a $\chi^{(3)}$ material (red).

of cross-phase-modulation in $\chi^{(2)}$ materials also enables a similar absorption probability with a five times smaller coupling rate, γ , compared to $\chi^{(3)}$ materials.

The probability of absorbing an incoming wave packet only depends on the ratio between mode a 's linewidth, γ , and the spectral width of the wave packet, Ω_G . Figure 3 plots the error in the one-photon state fidelity, $1 - F_1$, for a Gaussian wave packet with a storage time of $T/\tau_G = 14.4$. The different curves correspond to different loss rates, γ_L , which is assumed equal for all cavity modes. As seen in the figure, the error decreases much faster with increasing γ/Ω_G for $\chi^{(2)}$ materials than $\chi^{(3)}$ materials due to the absence of cross-phase-modulation. The curves flatten where the error becomes dominated by loss. Figure 3 also plots the error in the conditional one-photon state fidelity defined by $\bar{F}_1 \equiv F_1/\langle \bar{1} | \bar{1} \rangle$. \bar{F}_1 may be understood as the probability of the input and output states being identical given there was no loss because it corresponds to the fidelity calculated using the renormalized state $|\bar{1}\rangle/\sqrt{\langle \bar{1} | \bar{1} \rangle}$ [15]. The ideal scenario for lossy cavities is that the output wave packet is a scaled version of the input, $\xi_{out}(t) = \sqrt{\eta} \xi_{in}(t - T)$. For a given loss rate, γ_L , there is a corresponding value of η from which $\Lambda_n^{(k)}$ is calculated to achieve $\xi_{out}(t) \approx \sqrt{\eta} \xi_{in}(t - T)$, see Ref. [15] for details.

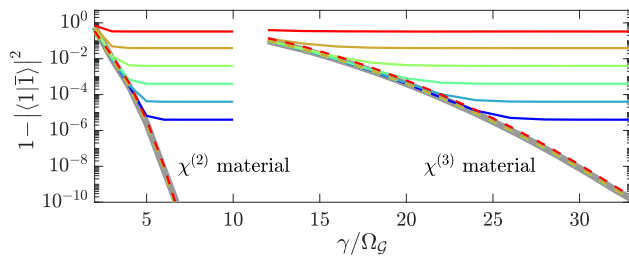


FIG. 3. Error in one-photon state fidelity, $1 - F_1$, as a function of the linewidth of mode a for different loss rates (solid lines). Gray corresponds to $\gamma_L/\Omega_G = 0$ while it increases from 10^{-7} (blue) to 10^{-2} (red) in steps of 10 dB. Dashed lines plot the corresponding error in the conditional one-photon state fidelity, $1 - \bar{F}_1$.

Since the conditional fidelity by definition is independent of the scaling factor η , we expect it to be negligibly dependent on loss so that $\bar{F}_1 \approx F_1(\gamma_L = 0)$, which is confirmed in Fig. 3. Thus, the photons will exhibit high visibility quantum interference with other photons in Gaussian wave packets if they are not lost. For increasing loss, it is always possible to achieve such high visibility at the cost of a corresponding decrease in η .

The *gate* fidelity is defined as the minimum *state* fidelity over all input states [14,19]. We can ensure that $F_1 \approx 1$ if γ/Ω_G is large enough, which means that the gate fidelity is given by F_{11} . Below, we choose $\gamma/\Omega_G = 6$ for $\chi^{(2)}$ materials and $\gamma/\Omega_G = 30$ for $\chi^{(3)}$ materials, which we see from Fig. 3 fulfills this requirement. The nonlinear interactions responsible for the conditional phase shift are described by the Hamiltonians

$$\hat{H}^{(2)} = \hbar \chi_2 (\hat{c} \hat{b}^\dagger \hat{b}^\dagger + \hat{c}^\dagger \hat{b} \hat{b}) \quad (2a)$$

$$\hat{H}^{(3)} = \hbar \chi_3 \left(\hat{a}^\dagger \hat{a} \hat{b}^\dagger \hat{b} + \frac{(\hat{a}^\dagger \hat{a} - 1) \hat{a}^\dagger \hat{a} + (\hat{b}^\dagger \hat{b} - 1) \hat{b}^\dagger \hat{b}}{4} \right), \quad (2b)$$

where \hat{c} is the annihilation operator for photons in the mode at $2\omega_b$ (see Fig. 1). The nonlinear coupling rates are [20,21]

$$\chi_2 = \sqrt{\frac{\hbar \omega_b \omega_b}{\epsilon_0 n^3}} \frac{\chi^{(2)}}{\sqrt{V_m^{(2)}}} \quad \text{and} \quad \chi_3 = \frac{3 \hbar \bar{\omega}^2 \chi^{(3)}}{2 \bar{n}^4 \epsilon_0 V_m^{(3)}}, \quad (3)$$

where $\bar{\omega}^2 = \sqrt{\omega_a \omega_b \omega_1 \omega_2}$, $\bar{n}^2 = \sqrt{n(\omega_a) n(\omega_b) n(\omega_1) n(\omega_2)}$, ϵ_0 is the vacuum permittivity, $\chi^{(k)}$ is the k th-order nonlinear susceptibility, and $V_m^{(k)}$ is the mode volume for k th-order interactions.

Figure 4(a) shows the error, $1 - F_{11}$, for a $\chi^{(3)}$ material as a function of storage time for different values of the cavity loss rate, γ_L . Note that for each storage time, T , the nonlinear coupling rate, χ_3 , was chosen to achieve the phase requirement mentioned above. Without loss, the error scales as $1 - F_{11} \propto 1/T^{2.0}$ and 99% fidelity is possible with $T/\tau_G < 30$. The dashed colored lines in Fig. 4(a) plot the conditional fidelity, $\bar{F}_{11} \equiv F_{11}/\langle \bar{1} | \bar{1} \rangle$. Note that $\bar{F}_{11} \approx F_{11}(\gamma_L = 0)$ as in Fig. 3, which means that $1 - \bar{F}_{11}$ may be understood as the error resulting from wave packet distortion alone, while $1 - F_{11}$ additionally includes error from loss. Increasing the storage time [beyond the optimum indicated by circles in Fig. 4(a)] reduces wave packet distortions at the cost of increased loss, resulting in a trade-off between the two error mechanisms.

Equation (3) can convert the normalized loss rate, $\tilde{\gamma}_L = \gamma_L/\Omega_G$, into an intrinsic quality factor, $Q_L = \omega/\gamma_L$. We do this using the parameters listed in the caption of Fig. 4 for a silicon cavity with an ultrasmall mode volume

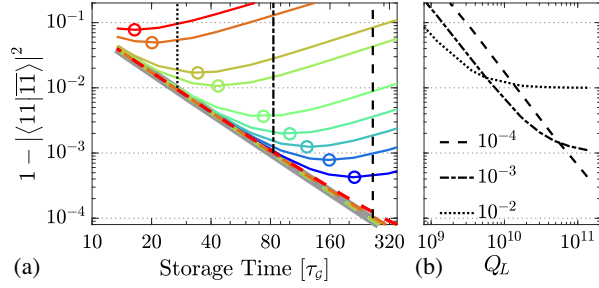


FIG. 4. (a) Plot of $1 - F_{11}$ for a $\chi^{(3)}$ material as a function of storage time, T , for different loss rates. Gray corresponds to $\gamma_L/\Omega_G = 0$ and it increases from 4×10^{-7} (blue) to 10^{-3} (red). Dashed lines with the same color plot the corresponding values of the error in conditional fidelity, $1 - \bar{F}_{11}$. (b) Plot of $1 - F_{11}$ as a function of the intrinsic quality factor, Q_L , corresponding to the vertical cross sections in (a). The legend shows the limiting values of the conditional fidelity, $1 - \bar{F}_{11}$. Parameters: $\gamma/\Omega_G = 30$, $\chi^{(3)} = 1.8 \times 10^{-19} \text{ m}^2/\text{V}^2$ [22], $\lambda = 1550 \text{ nm}$, $\bar{n} = 3.4$, $V_m^{(3)} = 10^{-3}(\lambda/\bar{n})^3$.

[23–25]. Figure 4(b) plots the error, $1 - F_{11}$, as a function of Q_L for the three vertical cross sections in Fig. 4(a) corresponding to three limiting values of the conditional fidelity. The error is dominated by loss where the curves are linear and becomes dominated by wave packet distortion where the curves saturate.

Figure 5(a) shows the error, $1 - F_{11}$, for a $\chi^{(2)}$ material as a function of storage time for different values of the cavity loss rate. Here, the nonlinear coupling rate, χ_2 , is adjusted so T corresponds to one Rabi oscillation of the SHG process. The error scaling is $1 - F_{11} \propto 1/T^{4.1}$, which is better than in Fig. 4(a) since the photons only interact when they are both in mode b , while they interact during the entire absorption and emission process through both cross- and self-phase-modulation for $\chi^{(3)}$ materials. For the optimum choice of T [indicated by circles in Figs. 4(a) and 5(a)], the error grows in proportion to the ratio between the loss rate and the nonlinear coupling, $1 - F_{11} = C^{(k)}\gamma_L/\chi_k$, where k again denotes the order of the nonlinear interaction. Figure 5(b) plots this relationship for both $\chi^{(2)}$ (blue) and $\chi^{(3)}$ materials (red). It also shows that the conditional error, $1 - \bar{F}_{11}$, follows the same relation but is 5.1 and 3.0 times smaller (dashed lines) for $\chi^{(2)}$ and $\chi^{(3)}$ materials, respectively. The error may then be related to the quality factor and mode volume by

$$1 - F_{11}^{(2)} = C^{(2)} \frac{\sqrt{\tilde{V}_m^{(2)}}}{Q_L} \quad \text{and} \quad 1 - F_{11}^{(3)} = C^{(3)} \frac{\tilde{V}_m^{(3)}}{Q_L}, \quad (4)$$

where $V_m^{(k)} = \tilde{V}_m^{(k)}(\lambda/n)^3$ and $C^{(k)} \propto C^{(k)}/\chi^{(k)}$. Table I lists the values of $C^{(k)}$ for the two most promising $\chi^{(2)}$ materials and the most common $\chi^{(3)}$ material, silicon. The table also lists the required intrinsic quality factor to achieve

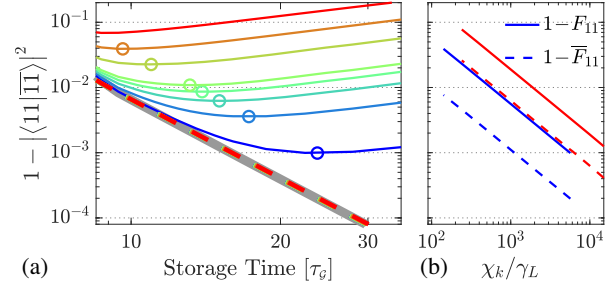


FIG. 5. (a) Plot of $1 - F_{11}$ for second-order nonlinearity as a function of storage time. Gray corresponds to $\gamma_L/\Omega_G = 0$ and it increases from 10^{-5} (blue) to 2×10^{-3} (red). Dashed lines with the same color plot the corresponding values of the error in conditional fidelity, $1 - \bar{F}_{11}$. (b) Plot of the minimum error as a function of χ_k/γ_L corresponding to the circles in Fig. 4(a) ($k = 3$, red) and Fig. 5(a) ($k = 2$, blue). Dashed lines plot the corresponding values of the conditional fidelity. The slope of all curves are -1 , demonstrating the relationship $1 - F_{11} = C^{(k)}\gamma_L/\chi_k$, where $C^{(2)} = 5.5$ and $C^{(3)} = 18.7$. Note that (a) and (b) share the y axis.

a conditional fidelity of 99% for an ultrasmall mode volume, $\tilde{V}_m^{(k)} = 10^{-3}$ [23–25], and a less demanding value of $\tilde{V}_m^{(k)} = 0.5$.

Towards practical implementations.—While the numbers in Table I are very challenging for $\chi^{(3)}$ materials, they are much closer to state-of-the-art LiNbO₃ devices. Quality factors of ring resonators have reached 10^7 [28,29] and 1D PHC cavities are currently at 10^6 [30,31]. Crossbar PHC designs (as shown in Fig. 1) have been demonstrated in GaAs [32,33], and show a path towards doubly-resonant cavities with resonances at ω_b and $2\omega_b$. Dynamically coupled cavities have been demonstrated using free-carrier dispersion [34,35] and frequency conversion between cavity modes (necessary for our coupling scheme) has been studied theoretically [36,37] and demonstrated experimentally [38–42].

From Fig. 2 it is evident that the control pulses and photon wave packets are of similar duration, which suggests that optical control fields are necessary, although electrical control has been demonstrated in LiNbO₃ [42].

TABLE I. Required values of the intrinsic quality factor to achieve a conditional fidelity of 99% for three relevant materials. The corresponding values of Q_L for a fidelity of 99% are 5.1 times larger for $\chi^{(2)}$ materials and 3.0 times larger for $\chi^{(3)}$ materials. Parameters: LiNbO₃: $\chi^{(2)} = 54 \text{ pm/V}$ [26], $\lambda = 1550 \text{ nm}$, $n = 2.1$. GaAs: $\chi^{(2)} = 270 \text{ pm/V}$ [27], $\lambda = 3100 \text{ nm}$, $n = 3.5$. Si: $\chi^{(3)} = 1.8 \times 10^{-19} \text{ m}^2/\text{V}^2$ [22], $\lambda = 1550 \text{ nm}$, $n = 3.4$.

	LiNbO ₃		GaAs		Si	
$C^{(k)}$	5.0×10^6		8.6×10^6		5.9×10^{10}	
$\tilde{V}_m^{(k)}$	10^{-3}	0.5	10^{-3}	0.5	10^{-3}	0.5
Q_L	3×10^6	7×10^7	5×10^6	10^8	2×10^9	10^{12}

Ultrafast pulse shaping [43] and time lenses [44] have demonstrated precise control of optical fields suggesting that pulses like $\Lambda^{(2)}$ in Fig. 2 could be synthesized with existing technology (note that $\tau_G \approx 200$ ps for $\bar{F}_{11} = 99\%$ and $\tilde{V}_m^{(2)} = 0.5$ in Fig. 2).

Thermo-refractive noise at room temperature in high Q/V cavities will limit the performance of Si-based gates but not the $\chi^{(2)}$ materials in Table I [45]. Assuming $\tilde{V}_m^{(2)} = \tilde{V}_m^{(3)}$, we find $\chi_2/\chi_3 \sim 10^5$ for LiNbO₃ ($\chi^{(3)} = 1.6 \times 10^{-21}$ m²/V² [46]) and $\sim 10^2$ for GaAs ($\chi^{(3)} = 2.0 \times 10^{-17}$ m²/V² [47]). Noise from higher-order nonlinear effects is therefore negligible for LiNbO₃ but should be included for GaAs.

Although many of the required cavity specifications have been reached with different components, more work is needed to demonstrate them in one device. Our work provides a practical architecture for combining them into deterministic two-qubit gates and establishes the progress necessary to achieve room-temperature quantum information processing.

The authors thank Joshua Combes and Jeffrey Shapiro for many useful discussions. This work was partly funded by the AFOSR Program No. FA9550-16-1-0391, supervised by Gernot Pomrenke (D. E.), the MITRE Quantum Moonshot Program (M. H. and D. E.), an ARL DIRA ECI grant (K. J.), and The Velux Foundations (M. H.).

Note added.—Recently, a similar concurrent study was also posted [48].

* mheuck@mit.edu

- [1] E. Knill, G. Milburn, and R. Laflamme, A scheme for efficient quantum computation with linear optics, *Nature (London)* **409**, 46 (2001).
- [2] P. Kok, W. J. Munro, K. Nemoto, T. C. Ralph, J. P. Dowling, and G. J. Milburn, Linear optical quantum computing with photonic qubits, *Rev. Mod. Phys.* **79**, 135 (2007).
- [3] J. H. Shapiro, Single-photon Kerr nonlinearities do not help quantum computation, *Phys. Rev. A* **73**, 062305 (2006).
- [4] J. Gea-Banacloche, Impossibility of large phase shifts via the giant Kerr effect with single-photon wave packets, *Phys. Rev. A* **81**, 043823 (2010).
- [5] B. He, A. MacRae, Y. Han, A. I. Lvovsky, and C. Simon, Transverse multimode effects on the performance of photon-photon gates, *Phys. Rev. A* **83**, 022312 (2011).
- [6] S. Xu, E. Rephaeli, and S. Fan, Analytic Properties of Two-Photon Scattering Matrix in Integrated Quantum Systems Determined by the Cluster Decomposition Principle, *Phys. Rev. Lett.* **111**, 223602 (2013).
- [7] J. Dove, C. Chudzicki, and J. H. Shapiro, Phase-noise limitations on single-photon cross-phase modulation with differing group velocities, *Phys. Rev. A* **90**, 062314 (2014).
- [8] T. C. Ralph, I. Söllner, S. Mahmoodian, A. G. White, and P. Lodahl, Photon Sorting, Efficient Bell Measurements, and a Deterministic Controlled-Z Gate Using a Passive Two-Level Nonlinearity, *Phys. Rev. Lett.* **114**, 173603 (2015).
- [9] D. J. Brod and J. Combes, Passive Cphase Gate Via Cross-Kerr Nonlinearities, *Phys. Rev. Lett.* **117**, 080502 (2016).
- [10] I. Iakoupov, J. Borregaard, and A. S. Sørensen, Controlled-Phase Gate for Photons Based on Stationary Light, *Phys. Rev. Lett.* **120**, 010502 (2018).
- [11] K. Xia, M. Johnsson, P. L. Knight, and J. Twamley, Cavity-Free Scheme for Nondestructive Detection of a Single Optical Photon, *Phys. Rev. Lett.* **116**, 023601 (2016).
- [12] B. Viswanathan and J. Gea-Banacloche, Analytical results for a conditional phase shift between single-photon pulses in a nonlocal nonlinear medium, *Phys. Rev. A* **97**, 032314 (2018).
- [13] D. V. Reddy and M. G. Raymer, Photonic temporal-mode multiplexing by quantum frequency conversion in a dichroic-finesse cavity, *Opt. Express* **26**, 28091 (2018).
- [14] A. Nysteen, D. P. S. McCutcheon, M. Heuck, J. Mørk, and D. R. Englund, Limitations of two-level emitters as nonlinearities in two-photon controlled-PHASE gates, *Phys. Rev. A* **95**, 062304 (2017).
- [15] M. Heuck, K. Jacobs, and D. R. Englund, accompanying paper, Photon-photon interactions in dynamically coupled cavities, *Phys. Rev. A* **101**, 042322 (2020).
- [16] V. Scarani, M. Ziman, P. Štelmachovič, N. Gisin, and V. Bužek, Thermalizing Quantum Machines: Dissipation and Entanglement, *Phys. Rev. Lett.* **88**, 097905 (2002).
- [17] F. Ciccarello, Collision models in quantum optics, *Quantum Meas. Quantum Metrol.* **4**, 53 (2017).
- [18] J. A. Gross, C. M. Caves, G. J. Milburn, and J. Combes, Qubit models of weak continuous measurements: Markovian conditional and open-system dynamics, *Quantum Sci. Technol.* **3**, 024005 (2018).
- [19] M. A. Nielsen and I. L. Chuang, *Quantum Computation and Quantum Information: 10th Anniversary Edition*, 10th ed. (Cambridge University Press, New York, NY, USA, 2011).
- [20] A. Majumdar and D. Gerace, Single-photon blockade in doubly resonant nanocavities with second-order nonlinearity, *Phys. Rev. B* **87**, 235319 (2013).
- [21] Z. Vernon and J. E. Sipe, Strongly driven nonlinear quantum optics in microring resonators, *Phys. Rev. A* **92**, 033840 (2015).
- [22] D. J. Moss, R. Morandotti, A. L. Gaeta, and M. Lipson, New CMOS-compatible platforms based on silicon nitride and Hydex for nonlinear optics, *Nat. Photonics* **7**, 597 (2013).
- [23] S. Hu and S. M. Weiss, Design of photonic crystal cavities for extreme light concentration, *ACS Photonics* **3**, 1647 (2016).
- [24] H. Choi, M. Heuck, and D. Englund, Self-Similar Nanocavity Design with Ultrasmall Mode Volume for Single-Photon Nonlinearities, *Phys. Rev. Lett.* **118**, 223605 (2017).
- [25] S. Hu, M. Khater, R. Salas-Montiel, E. Kratschmer, S. Engelmann, W. M. J. Green, and S. M. Weiss, Experimental Realization of Deep Subwavelength Confinement in Dielectric Optical Resonators, *Sci. Adv.* **4**, eaat2355 (2018).
- [26] C. Wang, X. Xiong, N. Andrade, V. Venkataraman, X.-F. Ren, G.-C. Guo, and M. Lončar, Second harmonic generation in nano-structured thin-film lithium niobate waveguides, *Opt. Express* **25**, 6963 (2017).
- [27] T. Skauli, K. L. Vodopyanov, T. J. Pinguet, A. Schober, O. Levi, L. A. Eyres, M. M. Fejer, J. S. Harris, B. Gerard, L.

- Becouarn, E. Lallier, and G. Arisholm, Measurement of the nonlinear coefficient of orientation-patterned GaAs and demonstration of highly efficient second-harmonic generation, *Opt. Lett.* **27**, 628 (2002).
- [28] M. Zhang, C. Wang, R. Cheng, A. Shams-Ansari, and M. Lončar, Monolithic ultra-high q lithium niobate microring resonator, *Optica* **4**, 1536 (2017).
- [29] B. Desiatov, A. Shams-Ansari, M. Zhang, C. Wang, and M. Lončar, Ultra-low-loss integrated visible photonics using thin-film lithium niobate, *Optica* **6**, 380 (2019).
- [30] H. Liang, R. Luo, Y. He, H. Jiang, and Q. Lin, High-quality lithium niobate photonic crystal nanocavities, *Optica* **4**, 1251 (2017).
- [31] M. Li, H. Liang, R. Luo, Y. He, J. Ling, and Q. Lin, Photon-level tuning of photonic nanocavities, *Optica* **6**, 860 (2019).
- [32] K. Rivoire, S. Buckley, and J. Vučković, Multiply resonant photonic crystal nanocavities for nonlinear frequency conversion, *Opt. Express* **19**, 22198 (2011).
- [33] S. Buckley, M. Radulaski, K. Biermann, and J. Vučković, Second harmonic generation in photonic crystal cavities in (111)-oriented GaAs, *Appl. Phys. Lett.* **103**, 211117 (2013).
- [34] Y. Tanaka, J. Upham, T. Nagashima, T. Sugiya, T. Asano, and S. Noda, Dynamic control of the Q factor in a photonic crystal nanocavity, *Nat. Mater.* **6**, 862 (2007).
- [35] Q. Xu, P. Dong, and M. Lipson, Breaking the delay-bandwidth limit in a photonic structure, *Nat. Phys.* **3**, 406 (2007).
- [36] P. Kumar, Quantum frequency conversion, *Opt. Lett.* **15**, 1476 (1990).
- [37] C. J. McKinstrie, J. D. Harvey, S. Radic, and M. G. Raymer, Translation of quantum states by four-wave mixing in fibers, *Opt. Express* **13**, 9131 (2005).
- [38] Y.-P. Huang, V. Velez, and P. Kumar, Quantum frequency conversion in nonlinear microcavities, *Opt. Lett.* **38**, 2119 (2013).
- [39] Q. Li, M. Davanco, and K. Srinivasan, Efficient and low-noise single-photon-level frequency conversion interfaces using silicon nanophotonics, *Nat. Photonics* **10**, 406 (2016).
- [40] X. Guo, C.-L. Zou, H. Jung, and H. X. Tang, On-Chip Strong Coupling and Efficient Frequency Conversion between Telecom and Visible Optical Modes, *Phys. Rev. Lett.* **117**, 123902 (2016).
- [41] M. Heuck, J. G. Koefoed, J. B. Christensen, Y. Ding, L. H. Frandsen, K. Rottwitt, and L. K. Oxenlowe, Unidirectional frequency conversion in microring resonators for on-chip frequency-multiplexed single-photon sources, *New J. Phys.* **21**, 033037 (2018).
- [42] M. Zhang, C. Wang, Y. Hu, A. Shams-Ansari, T. Ren, S. Fan, and M. Lončar, Electronically programmable photonic molecule, *Nat. Photonics* **13**, 36 (2019).
- [43] A. M. Weiner, Ultrafast optical pulse shaping: A tutorial review, *Opt. Commun.* **284**, 3669 (2011).
- [44] R. Salem, M. A. Foster, A. C. Turner, D. F. Geraghty, M. Lipson, and A. L. Gaeta, Optical time lens based on four-wave mixing on a silicon chip, *Opt. Lett.* **33**, 1047 (2008).
- [45] C. Panuski, R. Hamerly, and D. Englund, Fundamental thermal noise limits for high- Q/V optical microcavities, *Bull. Am. Phys. Soc.* (2020), <https://meetings.aps.org/Meeting/MAR20/Session/L27.9>.
- [46] C. Wang, M. Zhang, M. Yu, R. Zhu, H. Hu, and M. Loncar, Monolithic lithium niobate photonic circuits for Kerr frequency comb generation and modulation, *Nat. Commun.* **10**, 1 (2019).
- [47] J. M. Hales, S. Chi, T. Allen, S. Benis, N. Munera, J. W. Perry, D. McMorro, D. J. Hagan, and E. W. Van Stryland, Third-order nonlinear optical coefficients of Si and GaAs in the near-infrared spectral region, in *Conference on Lasers and Electro-Optics (CLEO)* (Optical Society of America, 2018), p. JTu2A.59.
- [48] M. Li, Y.-L. Zhang, H. X. Tang, C.-H. Dong, G.-C. Guo, and C.-L. Zou, Photon-photon quantum phase gate in a photonic molecule with $\chi^{(2)}$ nonlinearity, [arXiv:1909.10839](https://arxiv.org/abs/1909.10839).